M. D. Frederick, R. M. Gejji, J. E. Shepherd, and C. D. Slabaugh. Reactive processes following transverse wave interaction. Proceedings of the Combustion Institute, 2024. Preprint of article accepted for publication in the proceedings of the 40th International Symposium on Combustion, Milan, ITALY, July 21-26, 2024.

Reactive processes following transverse wave interaction

Mark D. Frederick[a,*], Rohan M. Gejji[a], Joseph E. Shepherd[b], Carson D. Slabaugh[a]

[a] *Purdue University, West Lafayette, IN 47907*
[b] *California Institute of Technology, Pasadena, CA, 91125*

Abstract

We examine two instances of transverse wave collision in a mixture of methane and oxygen diluted with 45% nitrogen. This mixture is classified near-limit and manifests a highly unstable structure. Simultaneous imaging of schlieren and broadband chemiluminescence was performed at a rate of 5 MHz to study the spatially- and temporally-coupled interactions between gas dynamic and chemical kinetic processes. Distinct modes of combustion are observed following transverse wave collision in each case. An unsteady reaction zone model is applied to understand the reactivity of the lead shock using measured values of the shock speed, acceleration, and curvature. In one case, an explosion behind the front immediately follows the creation of the new high-speed shock, which is an example of what is typically observed in detonation with regular cellular structure. Results of the model show that the high-speed shock directly initiates reaction before decaying and becoming non-reactive. In the other case, a reactive gas jet follows the high-speed shock, and no explosion occurs. The high-speed shock is unable to support reaction due to a combination of rapid deceleration and low shock speed. Analysis of the chemiluminescence field indicates that the reaction within the forward jet is supported by turbulent vortex structures and fresh reactants are provided along the shear layers between the high-speed shock and transverse wave. In each case a reverse jet is also observed that makes contact with unreacted gas pockets behind the front. The role of these jetting structures on wave propagation is discussed.

Keywords: Detonation; Transverse wave collision; Unsteady reaction zone; Hydrodynamic jet flow

Information for Colloquium Chairs and Cochairs, Editors, and Reviewers

1) Novelty and Significance Statement

The novelty of this research is the unsteady reaction zone analysis performed using data extracted from simultaneously acquired images of the gas dynamic and chemical kinetic field within a detonation. The imaging is performed at a rate of 5 MHz, which enables the oscillatory motion (velocity, acceleration, and curvature) of the leading front to be measured and used to model the reaction zone in an unsteady framework. Previously, due to the experimental challenge of quantifying such high-speed and unsteady flows, only qualitative or steady analysis was possible with exclusively experimental images. This research is significant because it focuses on the influence of hydrodynamic jetting structures on the reactivity of the flow, following transverse wave collision. These "jets" have long been understood to be present within detonations, but their importance has remained ambiguous. This study makes a novel and significant contribution through experimental examination of this issue.

2) Author Contributions

- MF's contributions: designed research, performed research, analyzed data, wrote the paper, edited the paper
- RG's contributions: designed research, performed research, edited the paper
- JS's contributions: designed research, wrote software, analyzed data, edited the paper
- CS's contributions: designed research, edited the paper, acquired funding

3) Authors' Preference and Justification for Mode of Presentation at the Symposium

The authors prefer **OPP** presentation at the Symposium, for the following reasons:

- There are many viewpoints regarding the role of "jetting" and a room-audience-level would be beneficial to discuss these.
- Results utilize an unsteady analysis of experimental data. Previous experimental analysis methods have been descriptive.
- This work does not rely on substantial background information. Videos clearly illustrate the phenomenon being studied.
- OPP presentation enables the videos from which data was extracted to be viewed and the dynamic phenomenon understood.

1. Introduction

Transverse wave motion and interaction are characteristic features of detonation propagation. As the transverse wave travels along the main shock front, shear layers and turbulent flow are generated. Upon collision with a counter-propagating wave and in mixtures and confinement situations that result in regular cellular patterns, a volume of shocked gas is produced that rapidly and completely combusts. In mixtures with irregular cellular structure, often observed in hydrocarbon fuels and unconfined situations, the collision process is often less uniform and results in a much more complex flow field. In general, there are a range of outcomes from transverse wave interactions and the current work explores some of these.

A particular feature of interest in transverse wave collisions is the "jet" flow observed first by Subbotin [1] in regular cellular structures. A jet occurs due to the motion (primarily along the symmetry axis) of gas away from the high-pressure stagnation region occurring on the axis of symmetry following transverse wave collision. This region consists of vortical structures resulting from the roll-up of the shear layers extending from the intersections of the transverse waves and leading shock front. Similar structures are observed in oblique reflection of inert shock waves [2]. In detonations, these structures create turbulent motion that may play a significant role in the combustion processes behind the front [3–5].

In addition to influencing the reaction processes behind the front, two-dimensional numerical simulations [6–10] have also shown that the presence of a strong forward jet perturbs the leading shock to form additional transverse waves and associated triple points. Mach and Radulescu [7] propose this process is a mechanism for sustaining irregular detonation propagation. Simulations by Sow *et al.* [11] examined the effect of the ratio of specific heats (γ), known to be important in nonreactive shock interactions, on the collision process and detonation front dynamics.

In this paper we examine two instances of transverse wave collision that exhibit very distinct outcomes. Simultaneous high-speed schlieren and chemiluminescence imaging enables quantification of the dynamics of the leading shock front. The acquired images are of sufficient spatial and temporal resolution to resolve the jet and details of the reaction zones. Reaction progress along select trajectories through the leading shock front are modeled and compared with the observations. The occurrence and potential role of the jet structure is discussed.

2. Experiment Description

2.1. Detonation Channel

Experiments were carried out in the *Narrow Channel Facility* (NCF), a rectangular channel (152.4 x 17.78 mm) developed at the Explosion Dynamics Laboratory at Caltech [12] and currently operated at Zucrow Laboratories. Detonations of premixed gases are directly initiated with an acetylene-oxygen driver to create a nominally two-dimensional detonation wave. Detailed information regarding the design, operation, and previous findings with this facility are available in earlier publications [12–17].

2.2. Diagnostics

Simultaneous schlieren and broadband chemiluminescence imaging measurements were performed at a rate of 5 MHz. The imaging region was located 3.1 m from the location of initiation and imaged through two 170 mm diameter quartz windows using two Shimadzu HPV-X2 cameras. The schlieren system consists of a pulsed (5 MHz) LED source, two f/10 parabolic mirrors, a bandpass filter centered around the LED emission spectra (Semrock FF01-640/20 BrightLine), a circular schlieren cutoff, and a custom camera lens. The integration time of both cameras was 110 ns. The camera used for broadband chemiluminescence imaging was outside of the schlieren beam path, angled at 9° to have a coincident field of view with the schlieren camera. Spatial calibration was performed using DaVis 8.4.0 to correct for the perspective introduced by the angled camera and to precisely overlay the schlieren and chemiluminescence images. The Shimadzu HPV-X2 detectors have a sensor size of 400 x 250 pixels. In this configuration, the field of view was 108 x 68 mm, yielding a spatial resolution of 3.7 pixels/mm.

2.3. Test condition

The mixture used in this study was stoichiometric methane-oxygen diluted with 45% nitrogen, CH_4-$2O_2$-$2.5N_2$, with an initial pressure and temperature of 18.8 kPa and 295 K, respectively. Table 1 lists various detonation parameters, which were calculated with the GRI3.0 reaction mechanism [18] and the Shock and Detonation Toolbox [19]. The reported values are the von Neumann pressure, temperature, and ratio of specific heats (P_{vN}, T_{vN}, γ_{vN}), the Chapman-Jouguet velocity and Mach number (U_{CJ}, M_{CJ}), the induction and exothermic lengths/time ($\Delta_{I/E}$, $\tau_{I/E}$) and the reduced activation energy (θ). This mixture is classified as highly unstable, based on the value of θ = 12.11 [13], and as near-limit because failure to initiate a propagating detonation was observed in 56% of the attempts at this condition.

3. Results and Analysis

3.1. Overview of cases

Two cases, (A) and (B), that represent very distinct transverse wave collision outcomes, from an extensive set of experiments, were subjected to detailed analysis. These cases were each individual shots of

Table 1: Calculated detonation parameters for a mixture of CH_4-$2O_2$-$2.5N_2$ with P_0=18.8 kPa, T_0 = 295 K, γ_0 = 1.38.

P_{vN} [kPa]	T_{vN} [K]	γ_{vN}	U_{CJ} [m/s]	M_{CJ}	Δ_I [mm]	τ_I [μs]	Δ_E [μm]	τ_E [ns]	θ
749	1664	1.22	2017	5.73	7.99	26.5	238	389	12.11

the experiment that were initiated at the same initial condition (see Table 1).

Images for case (A) are shown in Figure 1a-g. The schlieren and chemiluminescence fields are overlaid to allow for consideration of the coupled gas-dynamic and chemical-kinetic features. The schlieren is shown in gray-scale and the chemiluminescence is displayed on the normalized color scale provided in the lower left corner of Fig. 1. Videos of both cases are provided in the supplementary material (Vid. S1 and S2).

The wave structure entering the field of view in Fig. 1a captures the moment just before transverse wave collision, when two high-speed shocks surround a low-speed shock. In frame (b) the collision occurs and in frame (c) an explosion (i) is evident in the chemiluminescence. This explosion generates a new high-speed shock with attached reaction front. The high-speed shocks from frame (a) have also transitioned into low-speed shocks (ii) with decoupled reaction fronts. The first evidence of a jet is observable in frame (d), once the explosion has expanded outward. A concave structure within the gas pocket (iii) that separates from the front is formed by the reverse jet. These discrete pockets likely contain unreacted or weakly-reacting gas and are common features of cellular detonation that are expected to be quite large in unstable mixtures [20, 21]. Indication of the forward jet is more challenging to identify. However, potential evidence of a vortical structure (iv) is visible along the forming shear layer. In frame (e), the transverse wave that moves through the upper shear layer (v) appears partially reactive. The chemiluminescence intensity is elevated and the density fluctuations lessen downstream of the transverse wave. In contrast, the lower shear layer (vi) has no corresponding chemiluminescence signal and there is a flow structure within this region that is indicative of contained supersonic flow [22]. These regions (v,vi) ultimately separate from the front upon transverse wave collision and form unreacted gas pockets, like (iii). For region (v), the beginning of this process occurs with the transverse wave collision (vii) at the top of frame (f). A reverse jet is observed within the detached pocket (viii) (formerly region (v)) in frame (g).

A gradient and a velocity map of the leading shock front are shown in frames (h) and (i) of Fig. 1, respectively. The dotted lines in frame (i) correspond to the leading edges of the seven frames in (a)-(g).

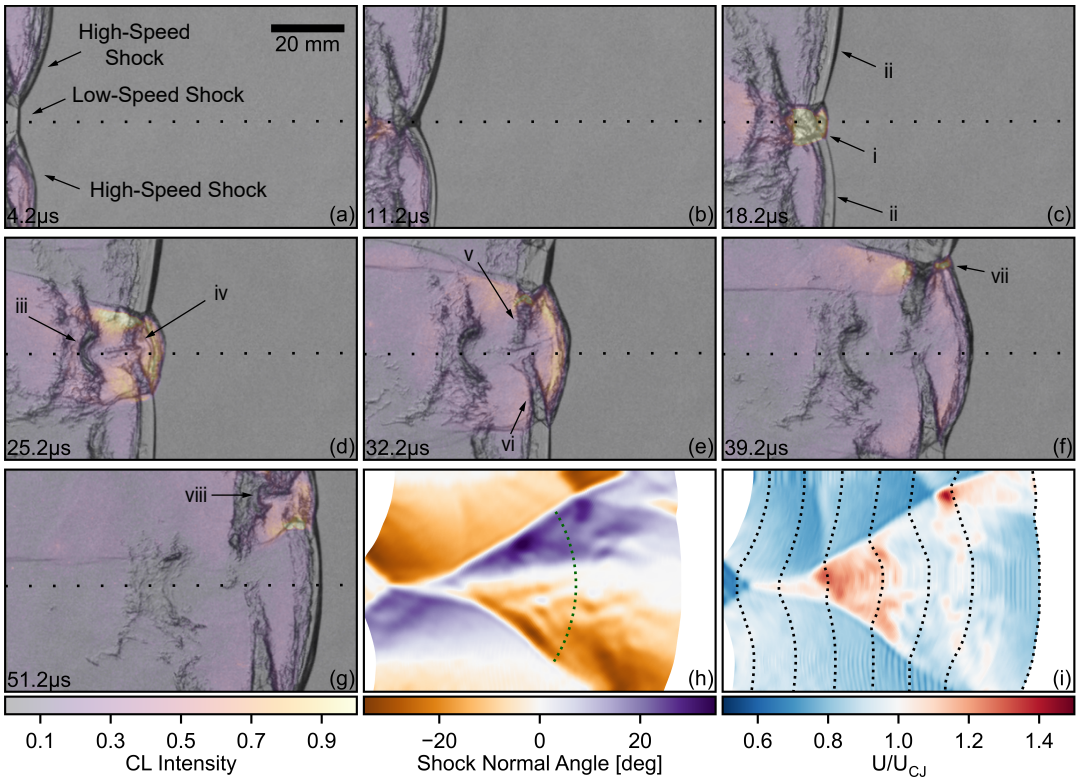

Fig. 1: Simultaneous schlieren and broadband chemiluminescence images of case (A) in frames (a)-(g) and the gradient and velocity map of the case in frames (h) and (i), respectively. The vertical running dotted lines on the velocity map correspond to the lead shock position of the displayed images. The horizontal dotted line in frames (a) - (g) marks the position for the parameter extraction in Fig. 3a and of the space-time diagram in Fig. 4.

The velocity map describes the spatial history of the wave, like a soot foil, but also captures the intrinsic velocity oscillation [17]. When the wave enters the field of view, all sections of it are moving below U_{CJ}, with the low speed shock considerably underdriven (U/U_{CJ} = 0.7). Note that the average wave speed measured with high-frequency pressure transducers indicate that the wave is globally propagating within 5% of U_{CJ}. For about 20 mm after transverse wave collision, between frames (b) and (c), the high-speed shock is moving near U_{CJ}, but not yet overdriven. After the explosion occurs at frame (c), the high-speed shock accelerates to U/U_{CJ} = 1.26 and the angle between the triple point tracks rapidly expands. By frame (e), the high-speed shock is no longer overdriven and the secondary transverse wave collision of frame (f) is registered as a period of rapid acceleration along the top of the velocity map.

Similarly for case (B), images (a-g), a gradient map (h), and a velocity map (i) are shown in Figure 2. When comparing to case (A) in Fig. 1, note that the chemiluminescence color scale has a lower maximum value because the peak intensity in case (B) is substantially lower than case (A). The structure entering the field of view is of two triple points moving toward each other prior to transverse wave collision. Triple-point (i) is traveling upward and (ii) is traveling downward. Between them is a low-speed shock moving at U/U_{CJ} = 0.6. Behind the low-speed shock is a well-defined keystone region [14] (iii) that contains shocked but unreacted material. In frame (b) the transverse wave collision process begins and a complex shock structure sets ups immediately behind the front in frames (c) and (d). In the portion of the velocity map between frames (c) and (d), the new high-speed shock is accelerated to speeds greater than U_{CJ}, but only remains overdriven for a distance of approximately 6 mm. Instead of the localized explosion that occurred in case (A), what follows the new high-speed shock (iv) is a distinct jet structure. The forward jet (v) develops through frame (g), which is the last frame captured. In the schlieren images, the forward jet is distinctly outlined and the only flow-feature that connects it to the leading front is the shear layer (vi) emanating from the lower triple-point (i). Chemiluminescence emission is contained within the boundary demarcated by the schlieren. The high-speed shock ahead of the forward jet appears nonreactive and smooth.

Appearing in concert with the forward jet is the reverse jet, which is also well resolved for this case. Unlike in case (A), where only the imprint of the reverse jet on the unreacted gas pocket served as evidence for its existence, the full structure of the reverse jet is resolved in the schlieren. In frame (e), the reverse jet (vii) begins to protrude into the unreacted

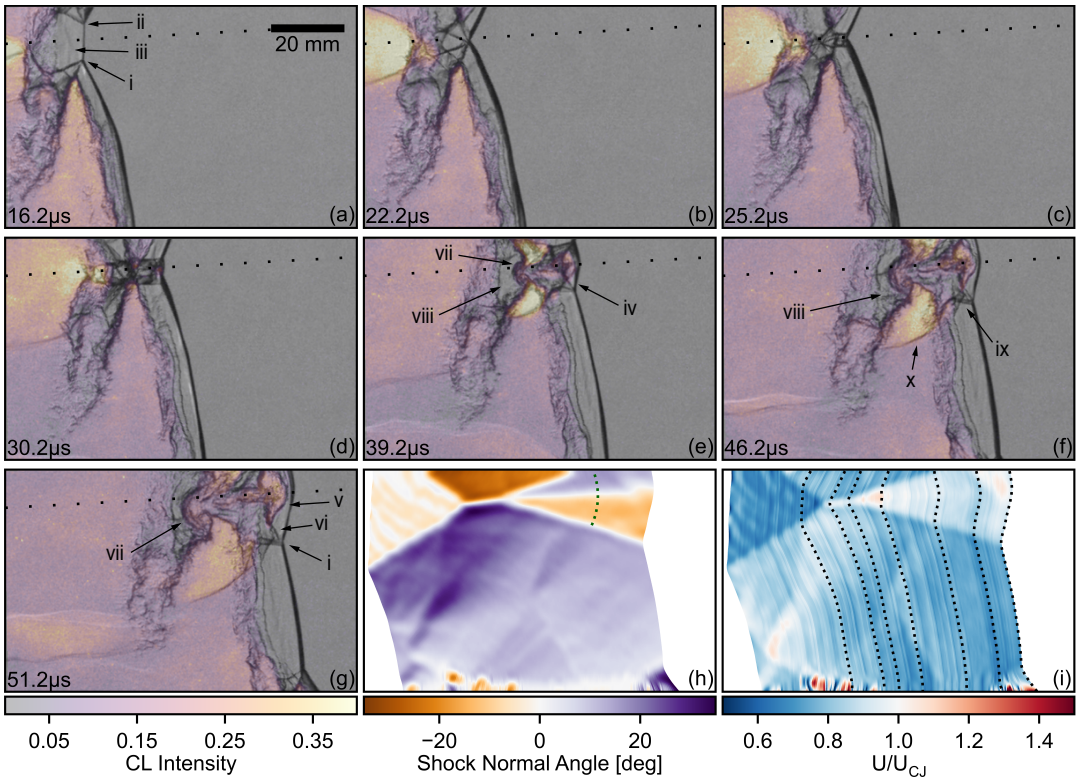

Fig. 2: Simultaneous schlieren and broadband chemiluminescence images of case (B) in frames (a)-(g) and the gradient and velocity map of the case in frames (h) and (i), respectively. The vertical running dotted lines on the velocity map correspond to the lead shock position of the displayed images. The horizontal dotted line in frames (a) - (g) marks the position for the parameter extraction in Fig. 3b and of the space-time diagram in Fig. 5.

gas volume (viii). As it expands backwards it convects combustion products, indicated by the chemiluminescence signal, into the unreacted gas pocket.

Newly formed transverse waves are the other prominent features of this case. The upper wave quickly exits the field of view, but the lower wave is captured in frames (e-g). The upstream section of the transverse wave (ix) moving through the shocked but unreacted region behind the low-speed shock in frame (g) is nonreactive. The downstream section (x) of the wave appears to be moving into reacted gas but there is a substantial increase in chemiluminescence intensity across the wave, indicating that either the upstream gas is only partially reacted or there are excited electronic states created by the wave.

3.2. Critical Decay Rate Model

In order to investigate the reactivity along the leading front and better understand the differences between cases (A) and (B), a model formulated by Eckett *et al.* [23] was used to simulate the reaction process behind an unsteady shock wave. This model is one-dimensional and can be used to predict the effect of unsteadiness on reaction progress and the critical value of shock wave unsteadiness (critical decay rate) that causes quenching. The model is formulated [24–26] in terms of the rate of change of temperature along a path line in the flow. An approximate evolution equation is

$$\frac{DT}{Dt} = -\frac{1}{c_v}\sum_n e_n \frac{W_n \dot{\omega}_n}{\rho} - \frac{RT}{c_v}\frac{1}{\tau_v}\,. \qquad (1)$$

A further approximation is to evaluate the volume expansion time τ_v immediately downstream of the shock wave for a given path line i by using the shock change equation

$$\frac{1}{\tau_v} = (-A\frac{\dot{\mathrm{U}}}{a_0} - Ba_0\kappa)_i \qquad (2)$$

where c_v is the constant volume specific heat, ρ is the density, R is the specific gas constant, and a_0 is the reactant sound speed, $\dot{\mathrm{U}}$ is the shock acceleration, and κ is the shock curvature. The species properties are: e_n, internal energy; W_n, molar mass; $\dot{\omega}_n$, net molar production rate.

The first term on the right-hand side of (1) is the chemical contribution to the temperature derivative. This is evaluated by summing over the contributions of all species in the reaction model and is large and positive when the reactions are exothermic. The second term term represents the contribution of flow divergence through a characteristic volume expansion time τ_v. There are two contributions to volume expansion. The first term of (2) is due to the shock wave unsteadiness and is always negative when the shock is decelerating. The second term of (2) is due to the wave curvature creating flow path expansion, this term is positive for $\kappa > 0$ and works to increase temperature in the same way that the static temperature of the flow increases through a quasi-1D subsonic diffuser [27]. Although the curvature effect is included in our analysis, the contribution of shock unsteadiness is a factor of five to ten times larger than that of the curvature throughout the duration analyzed of each case and wave curvature can be neglected without altering the ignition outcome, as was done in Eckett *et al.* [23].

A crucial assumption (discussed in Eckett et al. [23]) is that $\dot{\mathrm{U}}$ and κ remain constant along a given particle path i and can be evaluated at the instant a particle crosses the shock wave. The nondimensional coefficients A and B are computed using the shock change relations and are a function of shock speed U for a given mixture composition and initial conditions. The derivation of the model and details of the computation of A and B are provided in the Supplemental material.

Equation (1) and the species evolution equations are numerically integrated along particle paths starting from the frozen post-shock state of the initial mixture condition. The values of U, $\dot{\mathrm{U}}$, and κ are measured from the experimental data. A detailed reaction mechanism and realistic thermochemistry were used in these computations.

3.3. Shock Wave Parameter Evaluation

Figure 3 shows the normal shock velocity U and curvature κ evaluated when the shock front intersects the dotted extraction line in Figs. 1 and 2. For both cases the extraction line was selected to pass through the center of the newly formed high-speed shock and resolve its acceleration and deceleration. The velocity trace can be thought of as taking a 1D slice through the velocity map along the extraction line. The shock acceleration $\dot{\mathrm{U}}$ is computed as an average value between the red points that are superimposed on the velocity traces. An average value is used to avoid the error inherent in taking the second derivative of experimental data. In each case, the beginning of the averaging window coincides with the highest observed velocity. For case (A), $\dot{\mathrm{U}}$ = -63,200 km/s^2. For case (B), which has two distinct regions of deceleration, the acceleration from the first point to the second is $\dot{\mathrm{U}}_1$ = -91,100 km/s^2 and from the second to the third is $\dot{\mathrm{U}}_2$ = -16,400 km/s^2. The second point is chosen where there is a large inflection in the velocity trace.

The curvature κ trace reports the average value of curvature of the high-speed shock along the extraction line. This value is computed as the reciprocal of the radius found by fitting a circle to each extracted edge between the triple points. In case (B), when the upper triple-point leaves the field of view, all points above the lower triple-point are used for the fit. An example fit is shown as the green dotted curve in frame (h) of Figs. 1 and 2. Again an average value is used to avoid taking the second derivation of the spatial edge

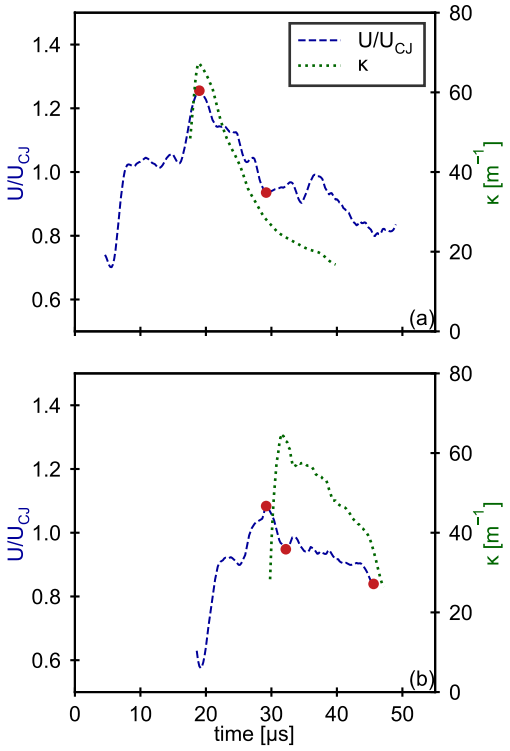

Fig. 3: Velocity and curvature traces extracted along the dotted lines shown Figs. 1 and 2. The sub-figure labels correspond to the case name. The red dots mark the points between which the average acceleration is computed.

coordinates. In case (A) (Fig. 3a) the largest value of κ corresponds to the peak in shock speed and then monotonically decays with U as the shock front becomes more planar. This trend is consistent with the U-κ relationships found in numerical simulation [28]. The peak in curvature for case (B) occurs just after the peak in velocity and decays at a slower rate.

3.4. Reaction Zone Modeling Results

A space-time diagram of the overlaid schlieren and chemiluminescence fields taken along the dotted extraction line in Fig. 1 is shown in Figure 4a for case (A). The vertical dotted lines represent the path of twelve particles and terminate when the particles intersect with the leading shock. At the moment of intersection the parameters U and κ are extracted from the traces in Fig. 3a and used as inputs into the CDR model, along with the average value of $\dot{U}$. Fig. 4b shows the resulting temperature profiles. All particles begin at the initial mixture temperature T_0 and are then brought to the post-shock frozen state ($\approx$ 2000 K), where the reaction zone computation begins. For the first seven particles the temperature sharply rises above the post-shock state, which signifies that an explosion has occurred. Once reaction develops, the assumptions that define the model breakdown and the profile is no longer physically representative. As the wave speed U decays and the expansion term exerts a greater effect on the temperature, the induction time, reported as the elapsed time to the maximum temperature derivative, of the particles grows; $0.64\,\mu$s for the first particle (i) and $5.07\,\mu$s for the seventh. By the eighth particle (viii), demarcated by the blue dashed line, the expansion term outcompetes the chemical term and the reaction is quenched. The shock speed is $1.07U_{CJ}$ at this point and if not for unsteady expansion, the induction time would be 6.8 μs. As an example, the trajectory of the particle is extended beyond the shock intersection in Fig. 4a. The path does not intersect a region of high chemiluminescence intensity, indicating that the particle does not burn, as the model predicts. Direct computation of the critical value of unsteadiness confirms that reaction will be quenched due to unsteadiness for particles entering the shock subsequent to path seven.

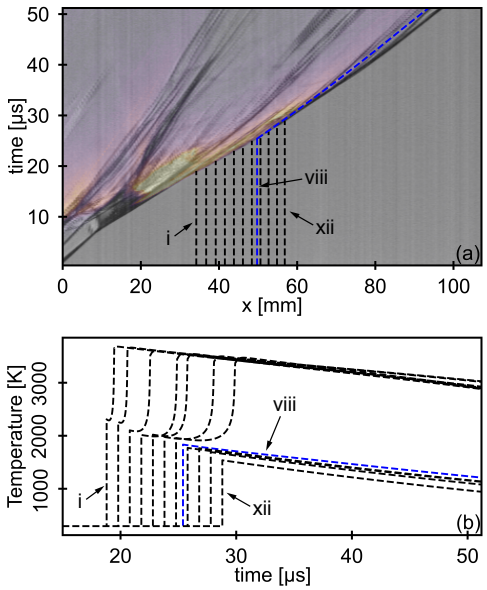

Fig. 4: Space-time diagram (a) of schlieren and chemiluminescence taken along the dotted extraction line in Fig. 1. The chemiluminescence color scale is the same as in Fig. 1. The vertical dashed lines in (a) represent particles and their corresponding temperature traces are shown in (b).

The same analysis is applied to case (B) along the seven particle paths shown in Figure 5a. The first four particles cross the lead shock within acceleration region $\dot{U}_1$ and the last three within $\dot{U}_2$ (see Fig.3b). None of these particles undergo direct initiation. As with particle (viii) of case (A), the first two particles here are moving faster than U_{CJ} when processed by the shock but unsteady expansion quenches the reaction. The lack of ignition along any of these particle paths confirms that the high-speed shock is nonreactive, as suggested by the lack of an attached chemiluminescence front (see Fig. 2g). Direct computation

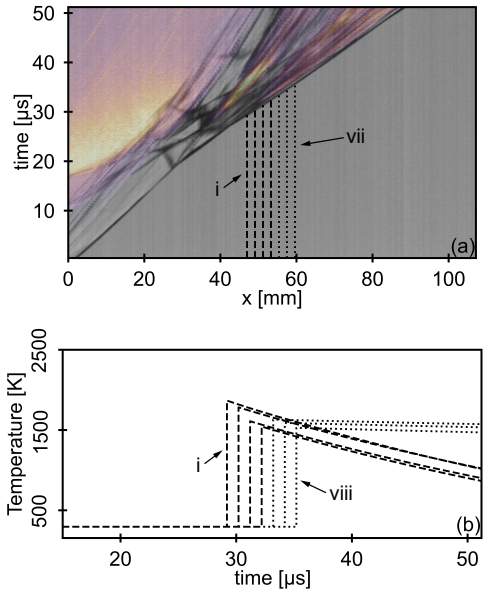

Fig. 5: Space-time diagram (a) of schlieren and chemiluminescence taken along the dotted extraction line in Fig. 2. The chemiluminescence color scale is the same as in Fig. 2. The vertical dashed lines in (a) represent particles and their corresponding temperature traces are shown in (b).

of the critical value of unsteadiness confirms that reaction will be quenched due to unsteadiness for all particles paths shown. Paths 1 and 7 are quenched but are close to the critical state.

4. Discussion

It is not immediately clear where the reaction contained within the forward jet originates. We first consider the possibility that the head of the jet serves to secondarily shock-compress and ignite the gas that has been previously compressed by the high-speed shock and remains unreacted. In frame (f) of Fig. 2 the speed of the high-speed shock along the extraction line is $0.85U_{CJ}$, which induces a post-shock particle velocity of 1444 m/s in the reference frame of the lab. Compared with the speed of the head of the jet at this moment, which we estimate as 1630 ± 130 m/s, it is clear that the strength of the jet is weak relative to the fluid it is moving through ($M \approx 0.26$). An estimate of the resulting induction time from this double-shock process is 750 μs, which is too long to explain the observed reaction. A visualization of the post-shock region with other techniques [29] could be helpful.

To better understand the reaction processes within the forward jet, the bottom row of Figure 6 shows a zoomed-in view of the isolated chemiluminescence field that encompasses the forward jet. In frame (f) at 27.2 μs, the first instance of reaction (i) is observed behind the new high-speed shock. This time coincides with the short period of super-U_{CJ} velocity that is measured in the velocity map of Fig. 2i, between 25.2 and 30.2 μs. This initial reaction is likely a result of direct initiation from the newly formed and accelerating high-speed shock. At 29.2 μs the first particle analyzed with the CDR model (Fig. 5b) predicts quenching. Therefore, the reaction that we see growing forward at 30.2 μs in Fig. 6g (and the subsequent frames) cannot be induced by the high-speed shock. In fact, the chemiluminescence intensity is nearly constant as the reactive forward jet structure grows, suggesting a constant reaction rate. It is our explanation that the subsequent reaction and flame growth within the jet is engendered by turbulent mixing of the products of ignition kernel (i) with unburned reactants that are entrained into the jet along the shear layer at the corner (feature (vi) in Fig. 2g). This is in line with the thoughts of previous authors who intuited the jet reactivity from schlieren images [1, 5].

To compare with case (A), the top row of Fig. 6 shows the reaction field in the moments leading up the explosion. Note that the maximum value of the chemiluminescence color scale used for case (A) in this figure is four time higher than case (B). Only 3.6 μs elapse from the first notice of ignition behind the high-speed shock (ii) in frame (a) until a clear explosion occurs in frame (d). The center of the explosion, feature (iii) in frame (c), is behind the location of the initial kernel (ii) and does not appear to be associated with any mixing induced by the forward jet.

5. Conclusion

The present study experimentally resolved the formation and growth of reactive processes following transverse wave collision. Specific attention was given to apparent gaseous jetting structures. In both cases, the role of the reverse jet seems evident, in that it carries products into the unreacted pockets behind the front, likely inducing some degree of burning therein. However, in both cases the pockets continue to exist after recording has ceased and further study is required to determine their fate. The role of the forward jet is more ambiguous. An unsteady reaction zone model was applied to estimate the reactivity of leading front ahead of the jetting structure. Experimentally measured values of shock speed, acceleration, and curvature were used to inform the model. For case (A), which is representative of what is typically observed following transverse wave collision in more stable mixtures, the model predicts that the leading shock will be reactive over a period of about 6 μs before unsteady effects quench the leading front. The forward jet may simply be a hydrodynamic reality and the auto-ignition of reactants further upstream dominates the events that follow. At the very least, if a forward jetting structure does play a role, it is not resolved in these images. For case (B), however, when the explosion event does not occur and the forward jet persists, it entrains unreacted gases and maintains and grows a flame through turbulent mechanisms. It is possible that this reaction supports the lead shock as a decoupled reacting region.

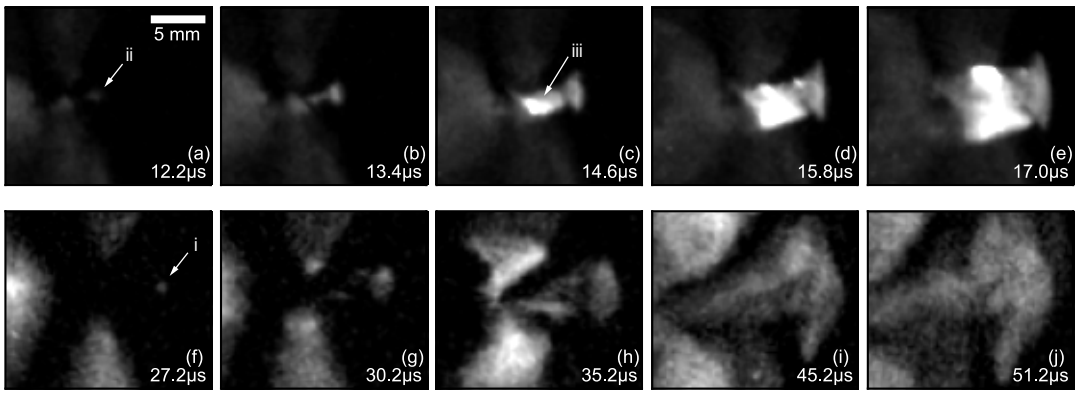

Fig. 6: Zoomed in view of the chemiluminescence intensity immediately after transverse wave collision for case (A) in frames (a-e) and case (B) in frame (f-j). The maximum value of the color scale for case (A) is four time higher than case (B).

Declaration of competing interest

The authors declare that they have no known competing financial interests or personal relationships that could have appeared to influence the work reported in this paper.

Acknowledgments

This work was supported by U.S. Air Force Office of Scientific Research grant FA9550-21-1-0013 (PO: Chiping Li). Mark D. Frederick acknowledges support from the National Science Foundation Graduate Research Fellowship Program under Grant No. DGE-1333468. One Shimadzu HPV-X2 used in this work was purchased with DURIP grant FA9550-20-1-0226 (PO: Chiping Li). The authors are grateful to Hadland Imaging for use of the second Shimadzu HPV-X2.

Supplementary material

Supplementary material associated with this article can be found in the online version.

References

[1] V. Subbotin, Collision of transverse detonation waves in gases, Combust. Explos. Shock Waves 11 (3) (1975) 411–414.

[2] G. Ben-Dor, Shock Wave Reflection Phenomena, 2nd Edition, Springer, Berlin, 2007.

[3] Y. Mahmoudi, K. Mazaheri, High resolution numerical simulation of triple point collision and origin of unburned gas pockets in turbulent detonations, Acta Astronaut 115 (2015) 40–51.

[4] R. Sorin, R. Zitoun, B. Khasainov, D. Desbordes, Detonation diffraction through different geometries, Shock Waves 19 (2009).

[5] R. R. Bhattacharjee, S. S. Lau-Chapdelaine, G. Maines, L. Maley, M. I. Radulescu, Detonation re-initiation mechanism following the Mach reflection of a quenched detonation, Proc. Combust. Inst. 34 (2) (2013) 1893–1901.

[6] G. J. Sharpe, Transverse waves in numerical simulations of cellular detonations, J. Fluid Mech 447 (2001) 31–51.

[7] P. Mach, M. I. Radulescu, Mach reflection bifurcations as a mechanism of cell multiplication in gaseous detonations, Proc. Combust. Inst. 33 (2011) 2279–2285.

[8] J. L. Ziegler, Simulations of Compressible, Diffusive, Reactive Flows with Detailed Chemistry Using a High-Order Hybrid WENO-CD Scheme, Ph.D. thesis, California Institute of Technology (2012).

[9] S. S. Lau-Chapdelaine, Q. Xiao, M. I. Radulescu, Viscous jetting and Mach stem bifurcation in shock reflections: Experiments and simulations, J. Fluid Mech. 908 (1986) (2020).

[10] P. A. Meagher, X. Shi, J. P. Santos, N. K. Muraleedharan, J. Crane, A. Y. Poludnenko, H. Wang, X. Zhao, Isolating gasdynamic and chemical effects on the detonation cellular structure: A combined experimental and computational study, Proceedings of the Combustion Institute 39 (3) (2023) 2865–2873.

[11] A. Sow, S. M. Lau-Chapdelaine, M. I. Radulescu, The effect of the polytropic index γ on the structure of gaseous detonations, Proc. Combust. Inst. 38 (3) (2021) 3633–3640.

[12] J. M. Austin, The role of instability in gaseous detonation, Ph.D. thesis, California Institute of Technology (2003).

[13] J. Austin, J. Shepherd, Detonations in hydrocarbon fuel blends, Combust. Flame 132 (1) (2003) 73–90.

[14] J. Austin, F. Pintgen, J. Shepherd, Reaction zones in highly unstable detonations, Proc. Combust. Inst. 30 (2) (2005) 1849–1857.

[15] M. D. Frederick, R. M. Gejji, J. E. Shepherd, C. D. Slabaugh, Preliminary Results from Narrow Channel Facility Experiments at Purdue University, in: AIAA Propulsion and Energy Forum, 2019, pp. 1–8.

[16] M. D. Frederick, R. M. Gejji, J. E. Shepherd, C. D. Slabaugh, Time-resolved imaging of the cellular structure of methane and natural gas detonations, Shock Waves 32 (2022) 337–351.

[17] M. D. Frederick, R. M. Gejji, J. E. Shepherd, C. D. Slabaugh, Statistical analysis of detonation wave structure, Proc. Combust. Inst. (2023) 2847–2854.

[18] G. P. Smith, D. M. Golden, M. Frenklach, M. W. Moriarty, B. Eiteneer, M. Goldenberg, C. T. Bowman, R. K. Hanson, S. Song, W. C. Gardiner, V. V. Lissianski, Z. Qin, GRI-Mech (Jul. 1999).
URL `www.me.berkeley.edu/gri_mech/`

[19] J. Shepherd, Shock and detonation toolbox (2018).
URL `https://shepherd.caltech.edu/EDL/SDT/`

[20] V. N. Gamezo, D. Desbordes, E. S. Oran, Two-

dimensional reactive flow dynamics in cellular detonation waves, Shock Waves 9 (1) (1999) 11–17.
[21] C. B. Kiyanda, A. J. Higgins, Photographic investigation into the mechanism of combustion in irregular detonation waves, Shock Waves 23 (2013) 115–130.
[22] S. R. Sanderson, J. M. Austin, Z. Liang, F. Pintgen, J. E. Shepherd, H. G. Hornung, Reactant jetting in unstable detonation, Progress in Aerospace Sciences 46 (2-3) (2010) 116–131.
[23] C. A. Eckett, J. J. Quirk, J. E. Shepherd, The role of unsteadiness in direct initiation of gaseous detonations, J. Fluid Mech 421 (2000) 147–183.
[24] J. E. Shepherd, Ignition modeling and the critical decay rate concept, Tech. rep., California Insistute of Technology, Pasadena (2019).
[25] M. I. Radulescu, B. M. Maxwell, Critical ignition in rapidly expanding self-similar flows, Physics of Fluids 22 (6) (2010).
[26] Y. Tan, R. Mével, Y. C. Liu, A review on ignition in expanding gaseous media, Process Safety and Environmental Protection 179 (2023) 241–256.
[27] W. Fickett, W. C. Davis, Detonation Theory And Experiment, Dover Puvlications, Mineola, New York, 1979.
[28] S. Jackson, C. Chiquette, M. Short, An intrinsic velocity–curvature–acceleration relationship for weakly unstable gaseous detonations, Proc. Combust. Inst. (2019) 3601–3607.
[29] S. B. Rojas Chavez, K. P. Chatelain, D. A. Lacoste, Two-dimensional visualization of induction zone in hydrogen detonations, Combustion and Flame 255 (2023).